



Inverse homogenization using isogeometric shape optimization

Lüdeker, Julian K.; Sigmund, Ole; Kriegesmann, Benedikt

Published in:
Computer Methods in Applied Mechanics and Engineering

Link to article, DOI:
[10.1016/j.cma.2020.113170](https://doi.org/10.1016/j.cma.2020.113170)

Publication date:
2020

Document Version
Peer reviewed version

[Link back to DTU Orbit](#)

Citation (APA):
Lüdeker, J. K., Sigmund, O., & Kriegesmann, B. (2020). Inverse homogenization using isogeometric shape optimization. *Computer Methods in Applied Mechanics and Engineering*, 368, Article 113170.
<https://doi.org/10.1016/j.cma.2020.113170>

General rights

Copyright and moral rights for the publications made accessible in the public portal are retained by the authors and/or other copyright owners and it is a condition of accessing publications that users recognise and abide by the legal requirements associated with these rights.

- Users may download and print one copy of any publication from the public portal for the purpose of private study or research.
- You may not further distribute the material or use it for any profit-making activity or commercial gain
- You may freely distribute the URL identifying the publication in the public portal

If you believe that this document breaches copyright please contact us providing details, and we will remove access to the work immediately and investigate your claim.

Inverse homogenization using isogeometric shape optimization

Julian K. Lüdeker^a, Ole Sigmund^b, Benedikt Kriegesmann^a

^a*Hamburg University of Technology, Am Schwarzenberg-Campus 4, 21073 Hamburg,
Germany*

^b*Technical University of Denmark, Solid Mechanics, Nils Koppels Allé, B.404, 2800
Kgs.Lyngby, Denmark*

Abstract

Finding periodic microstructures with optimal elastic properties is usually tackled by a highly resolved, regular finite element model and solid isotropic material penalization. This procedure has many advantages, but also requires a comparably high computational effort and challenges in representing stresses accurately. Therefore, an isogeometric shape optimization approach is applied to the inverse homogenization problem and combined with a reconstruction procedure for nearly optimal rank-3 laminates, which provides an efficient solution strategy with more accurate stress modelling. This allows to investigate the sensitivity of optimized microstructures in terms of stress concentrations.

Keywords: Inverse homogenization, Shape optimization, Isogeometric analysis, Optimal microstructures

1. Introduction

Designing periodic microstructures has become a fundamental research area in structural optimization. This topic is not only an important design tool itself, but it also helps reasoning the physical substance of interpolation schemes for material penalization approaches on a macroscopic scale [1], which have become one of the most successful tools in structural optimization [2]. In terms of elasticity problems, the optimality of theoretical bounds for the effective properties

Email address: julian.luedeker@tuhh.de (Julian K. Lüdeker)

(bulk/shear modulus) of composite microstructures is investigated in various works [3, 4, 5]. For practical applications, it is not practical to propose multi-scale laminates, whose performance exactly meet these bounds. Manufacturing and reliability become important issues and justify a loss of optimal performance. Bringing microstructures to applications for lightweight design does not only require optimization tools for both, simple featured structures on the micro-scale and the macro-scale, these procedures also have to be coupled [6]. Therefore, the one on the micro-scale has to be as efficient as possible. Decoupled projection procedures [7] benefit from simple featured microstructures, showing robustness against load aberrations.

Numerical homogenization. In order to determine the effective properties of microstructures, representative volume elements (RVEs) and periodic boundary conditions are used [8, 9, 10]. In combination with numerical, GALERKIN based methods it is possible to evaluate these properties for a given topology, containing multiple materials by the factorization of a single linear equation system.

Inverse homogenization. The basic idea to apply mathematical programming for the design of RVEs with optimized or prescribed properties, the so-called inverse homogenization problem, was first tackled by Sigmund [11, 12, 13] using lattice sizing and material penalization. This problem turns out to be highly nonunique. Consequently, the solution of the optimization strongly depends on the starting guess and the underlying parametrization. An efficient sizing parametrization using structural elements (e.g. bars, beams or plates) is limited in representing an optimized shape since it does not accurately model the fillets in between the elements and is only valid for small volume fractions. In contrast, topology optimization methods based on material penalization approaches are capable of representing almost any topology, depending on the mesh resolution and the regularization scheme. Notable disadvantages of this parametrization are the high computational cost and the huge impact of the starting guess due to local optima. These local optima may show nearly optimal performance,

but due to complex features, they appear to be sensitive to any kind of uncertainties and cause unnecessarily high manufacturing costs. Density-based approaches for inverse homogenization problem have been applied successfully to a various range of multi-physical problems; a review is given in [14]. In terms of elastic properties, the importance of the starting guess for two-dimensional problems is investigated by comparing different reasonable choices [15]. One of these starting guesses is created by a systematic reconstruction procedure for microstructures based on the moment representation for rank-N laminates [16, 17]. The reconstructed starting guess basically takes only two different topologies. For single loading cases, this procedure yields in a rank-2 microstructure, for multiple load cases a rank-3 microstructure (exemplarily shown in figure 1) is obtained. A density distribution representing this simple topology is mapped on a fixed, regular finite element (FE) mesh by use of projection approaches [7, 18]. Afterwards, a SIMP based topology optimization is applied, minimizing the complementary work. The resulting microstructures perform comparatively close to the theoretical bounds. Further, it is shown, that the topology does not change during the optimization by use of the proposed starting guess [15], if the ratio between volume fraction and minimum member size is chosen properly. Using relatively small filter radii may cause a split of initial members into multiple finer ones, resulting in so-called SIGMUND-structures and converging to the theoretical bounds [5].

Shape optimization. The topology maintaining starting guess for RVEs motivates the use of shape optimization procedures. Parameter-free shape optimization refers to approaches, where the optimization variables directly adjust the boundary of the design domain [19, 20]. Compared to sizing parametrizations the main benefits of parameter-free shape optimization is given by a less restricted design space. In comparison with material penalization approaches fewer design variables are required in order to represent smooth edges and the simulated stresses are more accurate since steplike contours are avoided [21]. The compromise is given by higher expenses for estimating the required gradi-

ent information, which also needs more intrinsic access to the simulation framework. The by far biggest disadvantage of these parametrizations is given in
70 form of mesh distortions due to big design changes, leading to numerical errors, which could be taken advantage of by the optimization procedure [22]. This is tried to be avoided by the introduction of different smoothing and regularization operations, yielding smooth boundaries but which also comes with a further limitation of the design space [23, 24, 25]. However, this is not mandatory if
75 one is starting from a good initial guess.

Isogeometric shape optimization. Most computer aided design (CAD) tools are build on non-uniform rational B-spline surfaces (NURBS) [26] or more advanced, similar spline representations (e.g. T-splines [27], U-splines). These splines allow a flexible and smooth description of complex geometries with a manageable
80 amount of control points. To directly use these geometric shape functions for simulations within a GARLERKIN framework, Hughes et. al. [28] illustrated the potential of so-called isogeometric analysis (IGA). Shape optimization and IGA have been combined in various works [29, 30, 31]. An overview of IGA based shape optimization is given in [32]. This procedure maintains a CAD compatible
85 geometry and reduces the number of design variables compared to classical finite element based shape optimization, but does not naturally overcome the issue of mesh distortions [25].

Contribution. The current paper aims at combining isogeometric shape optimization, inverse homogenization (similar to [33, 34, 35]) and a systematic way
90 of reconstructing a reasonable starting guess, resulting in nearly optimal, simple featured microstructures, in order to provide an efficient optimization procedure. The workflow of the proposed procedure is shown in figure 1. The accurate border of the IGA approach also allows investigating the high improvement in terms of stress concentrations during the optimization, even if the design changes and
95 the resulting improvement in terms of the objective function are comparably low. Finally, the sensitivity of the resulting designs will be investigated. Compared to the SIMP approach the proposed procedure only requires a small fraction

of degrees of freedom to represent optimized fillets and therefore applies well for computational expensive studies (e.g. multiscale/multiphysics optimization, robust formulations, etc.).

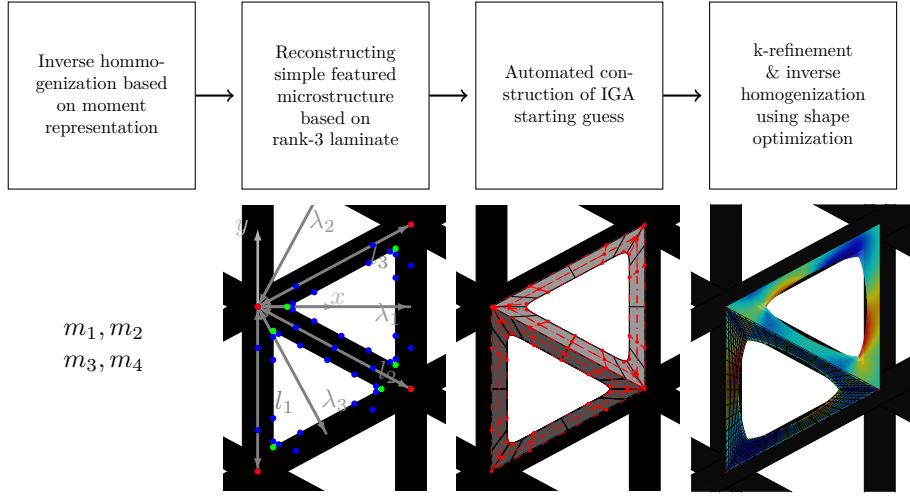


Figure 1: Workflow for IGA based inverse homogenization.

100

2. Isogeometric homogenization of single scale rank-3 laminates

This chapter provides a short introduction to the NURBS based IGA framework in terms of numerical homogenization, which is used for the optimization of simple featured rank-3 laminates.

105

2.1. Numerical homogenization

For linear elasticity, the properties of interest of the RVE are assembled in the symmetric 4th-order stiffness tensor. Generally, the effective stiffness tensor \mathbb{S}^H of a discretized RVE can be computed as:

$$\mathbb{S}^H = \frac{1}{V} \sum_{e=1}^{n_e} \int_{\Omega_e} (\boldsymbol{\varepsilon}^0 - \mathbf{B}_e \boldsymbol{\chi}_e)^T \mathbb{S}_e (\boldsymbol{\varepsilon}^0 - \mathbf{B}_e \boldsymbol{\chi}_e) dV = [\mathbb{C}^H]^{-1} \quad (1)$$

Here, $\boldsymbol{\varepsilon}^0$ represents an orthonormal basis of global test strain fields. The matrix \mathbf{B}_e describes the relation between local strain and nodal deformation and the

material tensor \mathbb{S}_e the relation between stress and strain for the e -th element. Here, Ω_e is the element domain, V is the RVE volume and n_e is the number of elements of the RVE. The correction displacement fields χ are resulting directly by applying these strain fields ε^0 in form of multiple volume forces, requiring the solution of multiple load cases \mathbf{P} .

$$\mathbf{K}\chi = \underbrace{\sum_{e=1}^{n_e} \int_{\Omega_e} \mathbf{B}_e \mathbb{S}_e \varepsilon^0 dV}_{\mathbf{P}} \quad (2)$$

Using periodic boundary conditions for all load cases decreases the number of factorizations for global stiffness matrices \mathbf{K} to one, since the lefthand-side of the linear equation system is constant if the boundary conditions are equivalent for all load cases.

110 *2.2. NURBS based isogeometric analysis*

IGA has become a generic term for a wide range of numerical methods, which have in common, that the system response \mathbf{u} ($= \chi$ in the homogenization community) is approximated by CAD compatible shape functions. In contrast to FEM, IGA does not simply fulfill C^1 -continuity of the shape functions on element but rather any desired continuity on the patch level [36], requiring few but fundamental changes in a numerical GARLERKIN framework [37, 38].

For a structured, two-dimensional control point grid \mathbf{X}_{ij} and corresponding weights w_{ij} , a NURBS surface \mathbf{N}_F (shown in figure 2) is defined as follows:

$$\mathbf{N}_F(\xi) = \frac{1}{W_F(\xi)} \sum_{i=1}^n \sum_{j=1}^m w_{ij} N_{i,p}^B(\xi_1) N_{j,q}^B(\xi_2) \mathbf{X}_{ij} \quad (3a)$$

$$W_F(\xi) = \sum_{i=1}^n \sum_{j=1}^m w_{ij} N_{i,p}^B(\xi_1) N_{j,q}^B(\xi_2) \quad (3b)$$

The required B-Spline N^B basis functions are given in Appendix A.

Consequently, the shape function for control point \mathbf{X}_{ij} , which is used for representing geometry and the physical system response is given by a product of two B-Spline basis functions.

$$N_{ij}(\xi) = \frac{1}{W_F(\xi)} w_{ij} N_{i,p}^B(\xi_1) N_{j,q}^B(\xi_2) \quad (4)$$

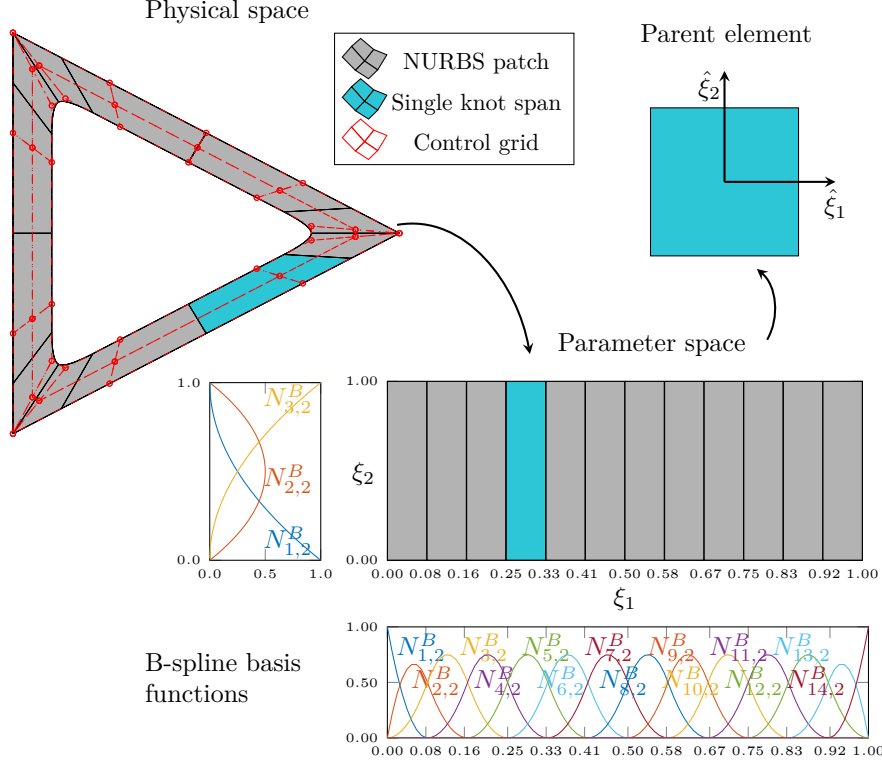


Figure 2: A single NURBS patch in physical and parameter space and the corresponding parent element for integration of a knot span.

For each control point \mathbf{X}_{ij} the matrix \mathbf{B} defines the linear relation between nodal displacements and strains at any local point $\boldsymbol{\xi}$ inside the NURBS. This matrix can be derived analogically to FEA [36], by transforming the local derivatives of the shape functions (which can be computed by use of the equations 3 and A.2) from the parameter space to the physical space (see figure 2), by use of the JACOBIAN \mathbf{J} .

$$\mathbf{B}_{ij}(\boldsymbol{\xi}) = \begin{bmatrix} \nabla_{X_1} N_{ij} & 0 \\ 0 & \nabla_{X_2} N_{ij} \\ \nabla_{X_2} N_{ij} & \nabla_{X_1} N_{ij} \end{bmatrix} \quad \nabla_{\mathbf{X}} N_{ij} = \mathbf{J}^{-1}(\boldsymbol{\xi}) \nabla_{\boldsymbol{\xi}} N_{ij} \quad (5)$$

The JACOBIAN of a knot span at a local position ξ can be derived analogically to FEA, by a sum over all control points that affect this knot span:

$$\mathbf{J}(\xi) = \sum_{ij=1}^{n_{npe}} \mathbf{X}_{ij} \otimes \nabla_\xi N_{ij} \quad (6)$$

The stiffness matrix of a knot span is computed by assembling all related \mathbf{B}_{ij} into \mathbf{B}_e and integrate over the element volume.

$$\mathbf{K}_e = \int_{\Omega_e} \mathbf{B}_e^T \mathbb{S}_e \mathbf{B}_e dV \quad (7)$$

The integration is performed by GAUSS-LEGRENDE quadrature¹ and requires an additional volumetric transformation. More efficient numerical integration schemes for NURBS based IGA are discussed in [39].

3. The inverse homogenization problem

The major optimization problem, discussed in this work seeks to minimize the complementary elastic work \mathcal{C} of a periodic microstructure for n_σ weighted stress states $\boldsymbol{\sigma}_I$ and a given volume fraction \tilde{f} .

$$\begin{aligned} \min_{\mathbf{v}} : \quad & \mathcal{C}(\mathbf{v}) = \frac{1}{2} \sum_{I=1}^{n_\sigma} w_I \boldsymbol{\sigma}_I : \mathbb{C}^H(\mathbf{v}) : \boldsymbol{\sigma}_I \\ \text{s.t.} : \quad & V(\mathbf{v}) - \tilde{f} \leq 0 \\ & : \quad \mathbf{v} \in \mathcal{V} \end{aligned} \quad (8)$$

¹¹⁵ The effective compliance tensor \mathbb{C}^H is computed by numerical homogenization (equation 1). The vector \mathbf{v} denotes the design variables within the feasible set \mathcal{V} .

3.1. Starting guess

Applying shape optimization to the inverse homogenization problem requires ¹²⁰ a qualified topology for the starting guess. This is achieved by combining the

¹Integration order is set to $m = 7$ for all considered numerical examples, yielding in 16 integration points per knot span.

moment representation of laminates (see Appendix B), a reconstruction procedure for rank-3 microstructures (see Appendix C and [15, 16, 17]) and an automated creation of representative CAD data based on NURBS. Generating IGA compatible meshes is limited in terms of automation, since not all CAD geometries are well suited and often require further pre-processing. One could create multiple CAD data, describing the same geometry, but result in different system responses by direct application of IGA [21]. Creating the CAD data starts from given layer spacings λ_i , layer orientations θ_i and relative layer contributions p_i . These data already hold all information to calculate the corner points of the RVE (red points in the second step of figure 1). The thickness of each layer $t_i = a(\tilde{f})p_i$ for a given volume fraction \tilde{f} is computed by use of a bisection algorithm [15]. Now the inner corners, indicated in green, can be estimated. All of the blue points are convex combinations of two corners. The red and the blue points represent the structured control grid of two second-order uniform B-Spline patches, indicated by different grey tones in the third step of figure 1, forming the complete RVE. The sharp outer corners are modelled by using the red points as double control points. Finally knot insertion [40, 41] is used to create a finer simulation grid. For all considered numerical examples, each of the initial knots is split in 4×4 knots, resulting in a total number of 1080 knots and 2630 degrees of freedom (DOF) for an accurate numerical model of a simple featured single-scale rank-3 microstructure (final step of figure 1). Compared to the regular FE mesh using 200×200 elements, resulting in 80802 DOF, the cost for solving equation 2 is strongly reduced.

3.2. Shape optimization: Parametrization

The term shape optimization covers a broad range of different parametrizations, having a significant impact on their capability to represent optimal shapes and therefore on the resulting structures [42]. Starting from an initial discretiza-

tion \mathbf{X}^0 of the shape, a general form of such problems is given by:

$$\begin{aligned} \min_{\mathbf{v}} : & f(\mathbf{X}, \mathbf{u}(\mathbf{X})) \\ \text{s.t.} : & c_i(\mathbf{X}, \mathbf{u}(\mathbf{X})) \leq 0 \quad i = 1, \dots, n_c \\ & \mathbf{R}(\mathbf{X}, \mathbf{u}(\mathbf{X})) = \mathbf{0} \\ & \mathbf{X} = \tilde{\mathbf{X}}(\mathbf{X}^0, \mathbf{v}) \end{aligned} \tag{9}$$

Here, f represents the objective function, c_i the constraints and \mathbf{R} the state equation of the optimization problem. The state equation is usually eliminated and considered in the gradient of the objective and constraint functions by direct or adjoint differentiation [43, 44], so it is solved separately for each iteration to obtain the physical response \mathbf{u} and appears to be the bottleneck for these kind of problems. The vector \mathbf{u} contains the nodal physical response of the system and \mathbf{X} describes nodal coordinates of the reference configuration of the simulation grid. Parametrizations for shape optimization differ in the choice of design variables \mathbf{v} and the corresponding mapping function $\tilde{\mathbf{X}}(\mathbf{X}^0, \mathbf{v})$, which is connecting the current reference configuration \mathbf{X} to the design variables [20]. This mapping may be a series of multiple functions, containing nodal movement, filtering and smoothing operations. Here, two properties for the mapping function are postulated. The first one ensures, that mapping the start vector of the design variables \mathbf{v}^0 results in the initial shape:

$$\mathbf{X}^0 = \tilde{\mathbf{X}}(\mathbf{X}^0, \mathbf{v}^0) \tag{10}$$

Secondly, $\tilde{\mathbf{X}}(\mathbf{X}^0, \mathbf{v})$ must be differentiable in \mathbf{v} since gradient based optimization algorithms are mandatory for an efficient procedure [45]. If that is the case, the gradient of any response function g (e.g. f, c_i, \mathbf{R}) with respect to the design variable can be computed by the chain rule:

$$\frac{\partial g}{\partial \mathbf{v}} = \frac{\partial g}{\partial \mathbf{X}} \frac{\partial \tilde{\mathbf{X}}}{\partial \mathbf{v}} \tag{11}$$

In the current work, the reference configuration is described by nodes, which equal control points in isogeometric analysis. The mapping function represents a movement of distance α_i for each node \mathbf{X}_i along a certain direction \mathbf{d}_i (figure

3). This direction is computed at the beginning of the optimization and kept constant. The distance of the movement of each node is directly depending on the design variables \mathbf{v} .

$$\tilde{\mathbf{X}}(\mathbf{X}^0, \mathbf{v}) = \mathbf{X}^0 + \text{diag}(\boldsymbol{\alpha}(\mathbf{v}))\mathbf{d} \quad (12)$$

The set of nodes $\mathbf{X}_i \in \mathcal{X} = \mathcal{X}_B \cup \mathcal{X}_I = \mathcal{X}_D \cup \mathcal{X}_F \cup \mathcal{X}_I$ are categorized as design nodes \mathcal{X}_D , fixed nodes \mathcal{X}_F and interior nodes \mathcal{X}_I (figure 3). Design nodes describe the unbounded border, fixed nodes the bounded border and interior nodes all the others that do not affect the boundary of the domain. Each design node $\forall \mathbf{X}_i \in \mathcal{X}^D$ is assigned to a single design variable v_i . The movement distance α_i for all nodes $\forall \mathbf{X}_i \in \mathcal{X}$ is a function of these variables. Introducing the filter operator \mathbf{F}_v , the relation of movement distance $\boldsymbol{\alpha}$ and design variables \mathbf{v} can be written as:

$$\boldsymbol{\alpha}_D = \mathbf{F}_v \mathbf{v}, \quad \boldsymbol{\alpha}_F = \mathbf{0}, \quad \boldsymbol{\alpha}_I = \mathbf{S}_I \mathbf{F}_v \mathbf{v} \quad (13)$$

These equations can be written in a condensed form:

$$\underbrace{\begin{bmatrix} \boldsymbol{\alpha}_D \\ \boldsymbol{\alpha}_F \\ \boldsymbol{\alpha}_I \end{bmatrix}}_{\boldsymbol{\alpha}} = \underbrace{\begin{bmatrix} \mathbf{I} \\ \mathbf{0} \\ \mathbf{S}_I \end{bmatrix}}_{\mathbf{S}} \mathbf{F}_v \mathbf{v} \quad (14)$$

Here, the matrix \mathbf{S}_I is connecting the movement of the interior nodes to the design variables, which is discussed in section 3.3. All above-mentioned matrices are kept constant, leading to a linear dependency between movement distance $\boldsymbol{\alpha}$ and design variables \mathbf{v} . The direction \mathbf{d}_i of each node is chosen as the normalized distance to the centre \mathbf{c}_p of the corresponding NURBS patch.

$$\mathbf{d}_i = \frac{\mathbf{c}_p - \mathbf{X}_i^0}{\|\mathbf{c}_p - \mathbf{X}_i^0\|} \quad (15)$$

The partial derivative of this mapping function is now given by a constant term:

$$\frac{\partial \tilde{\mathbf{X}}}{\partial \mathbf{v}} = \mathbf{S} \mathbf{F}_v \mathbf{d} \quad (16)$$

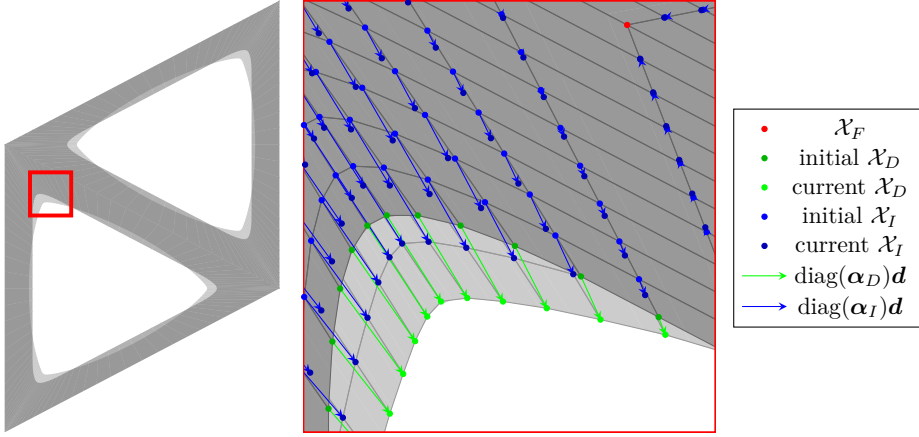


Figure 3: Illustration of the parametrization for shape optimization.

¹⁴⁵ *3.3. Shape optimization: Interior node movement*

The movement of interior nodes are defined by the matrix \mathbf{S}_I . Since NURBS patches are based on a structured control point grid and the RVEs are built in a way that every design node has a fixed node on its opposite side, the movement of the $i = 1, \dots, n_I$ interior nodes in between a fixed and a design node is linearly depending of the movement of the corresponding design node:

$$\alpha_I^j = S_I^{ji} \alpha_D^i \quad S_I^{ji} = \frac{i}{n_I + 1} \quad (17)$$

3.4. Shape optimization: Regularization

The filter matrix $\mathbf{F}_v = \mathbf{I}$ is representing an optional variable regularization. The used parametrization does not require a regularization scheme, if the starting guess is capable of representing a minimum. However if the initial step length is chosen comparably high, in order to perform less optimization iterations, it might be beneficial to introduce a regularization scheme to avoid the optimizer exploiting possible errors due to mesh distortions.

3.5. Shape optimization: Sensitivity analysis

This section focuses on estimating the gradient in dependence of a changing reference coordinate X_k for the complementary work \mathcal{C} . Starting from the objective function in problem 8, the gradient of \mathcal{C} is given by:

$$\frac{\partial \mathcal{C}}{\partial X_k} = \frac{1}{2} \sum_{i=1}^{n_\sigma} w_i \boldsymbol{\sigma}_i : \frac{\partial \mathbb{C}^H}{\partial X_k} : \boldsymbol{\sigma}_i \quad (18)$$

The gradient of the homogenized compliance tensor \mathbb{C}^H can be derived from its inverse \mathbb{S}^H by:

$$\frac{\partial \mathbb{C}^H}{\partial X_k} = - [\mathbb{C}^H]^T \frac{\partial \mathbb{S}^H}{\partial X_k} \mathbb{C}^H \quad (19)$$

The required gradient of the homogenized stiffness matrix is derived in Appendix D and is given by:

$$\begin{aligned} \frac{\partial \mathbb{S}^H}{\partial X_k} &= \frac{1}{V} \sum_{i=1}^{n_e} \sum_{j=1}^{n_g} (\boldsymbol{\varepsilon}^0 - \mathbf{B}_j \boldsymbol{\chi})^T \mathbb{S}_i (\boldsymbol{\varepsilon}^0 - \mathbf{B}_j \boldsymbol{\chi}) \frac{\partial \det J_j}{\partial X_k} w_j \\ &\quad - \left[\boldsymbol{\chi}^T \frac{\partial \mathbf{B}_j^T}{\partial X_k} \mathbb{S}_i (\boldsymbol{\varepsilon}^0 - \mathbf{B}_j \boldsymbol{\chi}) + (\boldsymbol{\varepsilon}^0 - \mathbf{B}_j \boldsymbol{\chi})^T \mathbb{S}_i \frac{\partial \mathbf{B}_j}{\partial X_k} \boldsymbol{\chi} \right] \det J_j w_j \end{aligned} \quad (20)$$

155 3.6. Shape optimization: Solution algorithm

All shape optimizations are solved by a MATLAB implementation of the original method of moving asymptotes (MMA) [46]. The subproblem of each iteration is solved by the interior point method [47] of the MATLAB optimization toolbox. MMA parameters are kept constant for all examples and given in table 160 1. The initial move limit is chosen relatively small. This choice depends on the lower and upper bounds for the design variables, set to ± 0.5 . These values affect the stability of the optimization procedure. However, the bounds are not reached for any design variable and therefore do not restrict the design space for any of the examples.

initial move limit	decreasing factor	increasing factor	maximum iterations
10^{-2}	0.7	1.2	50

Table 1: Parameters used for the method of moving asymptotes.

¹⁶⁵ **4. Numerical examples**

According to [48, 15], the regarded example is aiming at solving problem (8) considering $n_\sigma = 4$ stress states shown in figure 4. This problem is solved for different values of $\chi \in [0, 1]$ affecting the corresponding weights w_i between pure uniaxial ($\chi = 0$) and pure shear ($\chi = 1$) loading.

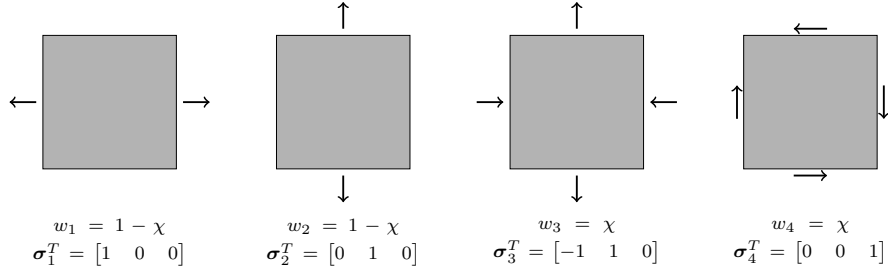


Figure 4: Load cases σ_i for the inverse homogenization problem and dedicated weights $w_I(\chi)$.

¹⁷⁰ The reference solution for this problem can be estimated by the moment formulation given in Appendix B and is shown for different volume fractions in figure B.8. This solution corresponds to a non-physical multi-scale rank-3 laminate. Reconstructing a single-scale microstructure comes with a loss of performance. Figure 5 illustrates the objective values (complementary work \mathcal{C}) for ¹⁷⁵ different uniaxial/shear ratios χ . Normalized denotes that the value is divided by the reference solution value. The performance of the reconstructed starting guess is already very close (below 10%) to the reference solution. Applying the presented shape optimization procedure further decreases the the aberration to the reference to below 5% as compared to 8% reported for regular SIMP ¹⁸⁰ parametrization in [15]. The initial and optimized shapes are illustrated in figure 6a.

Figure 6 also shows the von Mises-stress distribution² σ_{VM} for different uniaxial/shear ratios before and after the shape optimization. All considered

²Evaluation of the local stress fields using IGA and definition of stress measures is briefly discussed in Appendix E

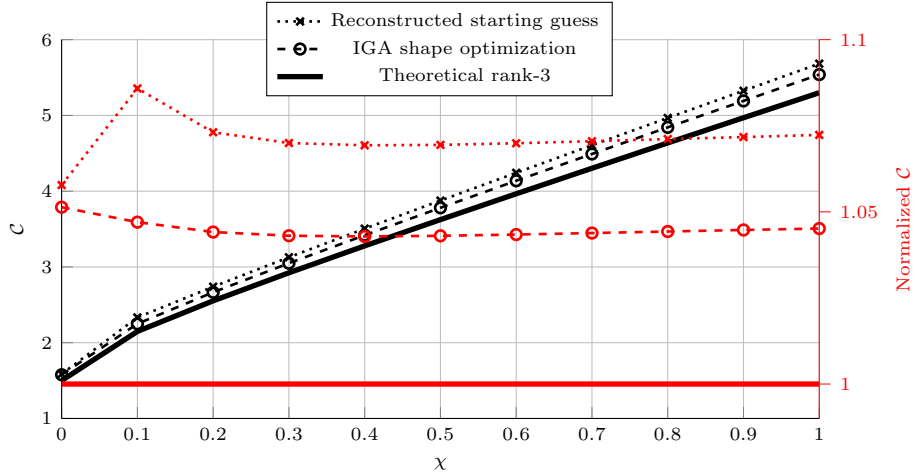


Figure 5: Complementary work scaled by the rank-3 energy bound for a constant volume fraction $\tilde{f} = 0.5$.

examples result in high stress peaks around the corners of the RVE, even if the starting guess already features smooth fillets. During the optimization procedure these peaks are drastically reduced. Even if the performance in terms of the objective function is only increased by less than 3%, the maximum stress peaks are reduced by up to 35%. The layouts of the optimized RVEs match the results achieved by the SIMP approach [15], featuring more sharp corners compared to the starting guess for higher values of χ . Contrary to intuitive expectations, the sharp corners of the optimized designs are not only beneficial in terms of the objective, but also reduce the stress concentrations. This is the case, if at least one layer is compressed and another is under tension and matches the results obtained by VIGDERGAUZ-like microstructures [49].

195 4.1. Robustness analysis of optimized microstructures

To further illustrate the benefits of the shape optimization step of the proposed procedure, a simple robustness analysis is performed. Therefore, a MONTE-CARLO simulation is applied to the evaluation of the local stress field. The random input for this simulation are the weighting factors w_I of the applied stress states σ_I , which are only affecting the post-processing, requiring only

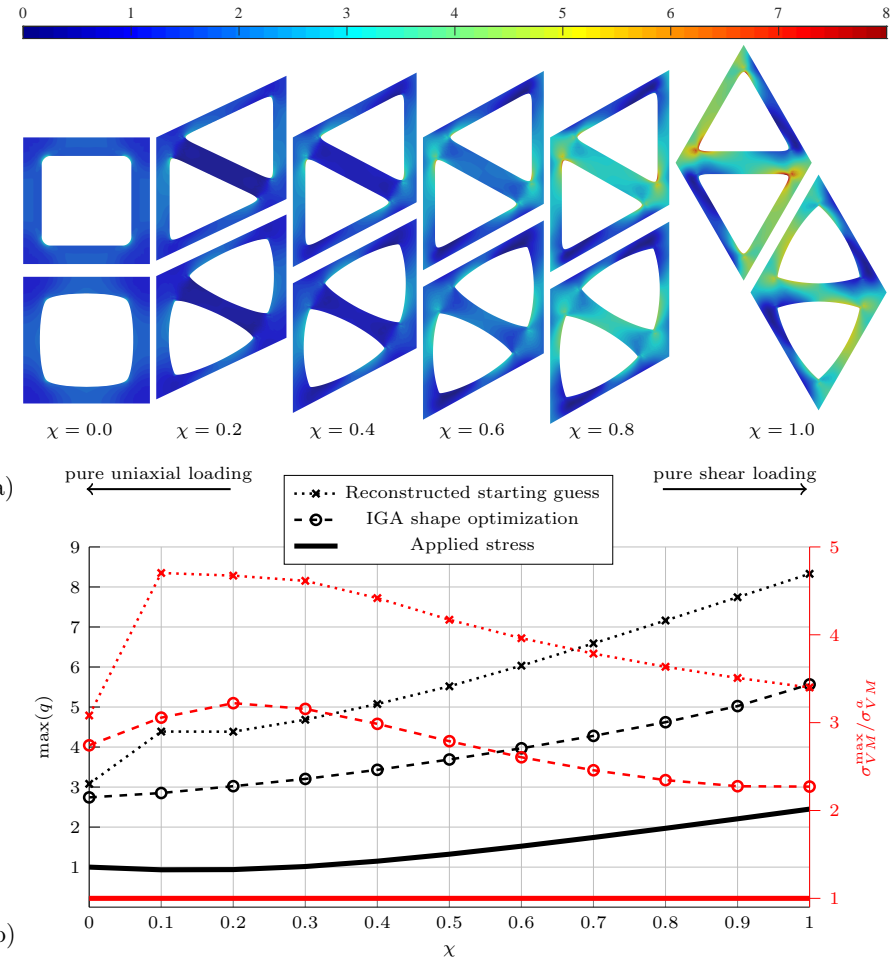


Figure 6: a) VON MISES-stress distribution for the reconstructed starting guess (top) and after the shape optimization step (bottom), b) Maximum VON MISES-stress σ_{VM}^{max} and stress concentration factor along χ , volume fraction $\tilde{f} = 0.5$.

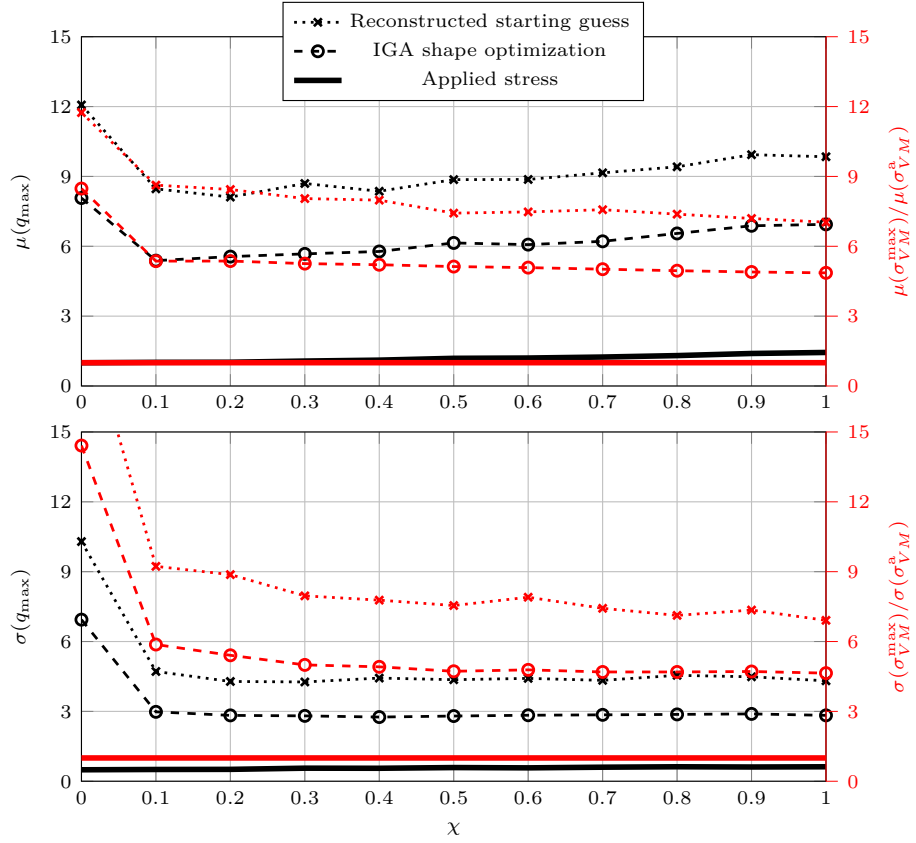


Figure 7: Mean value and standard deviation of the maximum VON MISES-stress for scattering weights around $\Delta w = \pm 0.5$ using $n=1000$ samples.

small additional computational effort. All four weight factors (defined in figure 4) are chosen to scatter independently following uniform distribution with $\Delta w_I = \pm 0.5$ ($w_I = w_I^0 + \Delta w_I \in [0, 1]$).

Mean value and the standard deviation of the maximum local stress subject to scattering weight factors are shown and compared to the scattering of the applied stress in figure 7. Both are significantly reduced by the shape optimization. Especially for the pure uniaxial load case $\chi = 0$, the mean value for the maximum stress shows a strong abberation to the deterministic one. Compared to the mixed load cases this abberation is much higher, since only the uniaxial load case is resulting in a rank-2 microstructure, which is not suitable for shear

bearing enforced by scattering of the applied stress.

5. Conclusions

This paper presents a numerically efficient procedure of finding nearly optimal single-scale microstructures using IGA based shape optimization. Compared to material penalization procedures, the degrees of freedom per iteration are drastically reduced. The use of IGA allows a detailed investigation of the local stress distribution. Applying shape optimization to the reconstructed starting guess comes only with a small improvement in terms of performance, but the local stress peaks are strongly decreased (up to 35%), even though they are not directly considered within the problem formulation. Furthermore, the optimized structures are less sensitive to load uncertainties.

The proposed IGA based shape optimization procedure is not suitable for capturing large design changes without further extensions. Therefore, using a less qualified starting guess typically results in strong mesh distortion. There are multiple strategies to avoid such problems. The most recommended strategy for the purpose of finding nearly optimal microstructures is to introduce a remeshing rule or mesh optimization when the mesh quality decreases rapidly. Another possibility is to involve filtering techniques, e.g. using a coarse NURBS mesh for the geometry and a refined, but equivalent mesh for the simulation or filtering techniques used in classical finite element based shape optimization. The mesh quality could also be constrained within the optimization problem. However, filtering or constraining the optimization problem always comes at the cost of more restricted and limited design space.

Future works will focus on the extension to 3D microstructures. Here, determining a systematic way for finding qualified starting guesses appears to be more cumbersome, but the benefits in terms of computational effort are even more important than in 2D. Furthermore, it is worth investigating whether embedding stress constraints and probabilistic analyses in the optimization procedure provides different optimized microstructures. The ultimate purpose of this

Acknowledgments

JL and BK acknowledge the funding by the TUHH college of excellence, co-funded by Airbus. OS acknowledges support through a Villum Investigator grant “InnoTop” from the Villum Fonden. JL is also grateful for the hospitality and rewarding research environment, given by the members of DTU’s TopOpt group.

²⁴⁰ procedure is to provide a systematic way to find qualified and simple featured CAD geometries for nearly optimal microstructures and providing a reasoned knowledge about their uncertainties.

Appendix A. B-Spline basis functions for NURBS

An extensive overview of B-Splines and NURBS is given in [26]. For a given knot vector ξ , NURBS of order p are based on the B-Spline basis functions $N_{i,p}^B$, which are computed recursively:

$$N_{i,0}^B(\xi) = \begin{cases} 1 & \text{if } \xi_i \leq \xi < \xi_{i+1} \\ 0 & \text{otherwise} \end{cases} \quad (\text{A.1a})$$

$$N_{i,p}^B(\xi) = \frac{\xi - \xi_i}{\xi_{i+p} - \xi_i} N_{i,p-1}^B(\xi) + \frac{\xi_{i+p+1} - \xi}{\xi_{i+p+1} - \xi_{i+1}} N_{i+1,p-1}^B(\xi) \quad (\text{A.1b})$$

The k -th derivative in terms of the local coordinate ξ can be computed by:

$$\frac{\partial^k N_{i,p}^B}{\partial^k \xi} = \frac{p!}{(p-k)!} \sum_{j=0}^k \alpha_{k,j} N_{i+j,p-k}^B(\xi) \quad (\text{A.2a})$$

$$\alpha_{0,0} = 1 \quad (\text{A.2b})$$

$$\alpha_{k,j} = \frac{\alpha_{k-1,j} - \alpha_{k-1,j-1}}{\xi_{i+p+j-k+1} - \xi_{i+j}} \quad j = 1, \dots, k-1 \quad (\text{A.2c})$$

245

Appendix B. Moment representation for rank-N laminates

The moment representation of laminates has been discussed in detail [16, 17, 48, 15] and is added for completeness. A rank-N laminate based on two materials with material properties $\mathbb{C}_+(E_+, \nu_+)$ and $\mathbb{C}_-(E_-, \nu_-)$ (one can be void) can be described by the layer orientations of the stiff material θ_i ($i = 1, \dots, N$) and the corresponding relative contribution p_i , which is equivalent to the layer thickness. The number of variables to describe the effective material properties of rank-N laminates can be reduced to four moments:

$$\begin{aligned} m_1 &= \sum_{i=1}^N p_i \cos(2\theta_i), & m_2 &= \sum_{i=1}^N p_i \sin(2\theta_i) \\ m_3 &= \sum_{i=1}^N p_i \cos(4\theta_i), & m_4 &= \sum_{i=1}^N p_i \sin(4\theta_i) \end{aligned} \quad (\text{B.1})$$

The feasible set of moments is given by:

$$\mathcal{M} = \mathbf{m} \in \mathbb{R}^4$$

$$\text{s.t. } \begin{cases} m_1^2 + m_2^2 - 1 \leq 0 \\ m_3 - 1 \leq 0 \\ -1 - m_3 \leq 0 \\ 2m_1^2(1 - m_3) + 2m_2^2(1 + m_3) + m_3^2 + m_4^2 - 4m_1m_2m_4 - 1 \leq 0 \end{cases} \quad (\text{B.2})$$

Further, the effective compliance tensor can be written as a function of these moments:

$$\mathbb{C}_H(\mathbf{m}) = \mathbb{C}_+ - (1 - \tilde{f}) \left[(\mathbb{C}_+ - \mathbb{C}_-)^{-1} - f E_+ \mathbb{S}_m(\mathbf{m}) \right]^{-1} \quad (\text{B.3a})$$

$$\mathbb{S}_m^{V^{oigt}}(\mathbf{m}) = \frac{1}{8} \begin{bmatrix} 3 + m_3 - 4m_1 & 1 - m_3 & -2m_2 - m_4 \\ 1 - m_3 & 3 + m_3 + 4m_1 & -2m_2 + m_4 \\ -2m_2 - m_4 & -2m_2 + m_4 & 1 - m_3 \end{bmatrix} \quad (\text{B.3b})$$

Using this representation allows to reformulate the inverse homogenization problem (8):

$$\min_{\mathbf{m}} : \mathcal{C}(\mathbf{m}) = \frac{1}{2} \sum_{i=1}^{n_\sigma} w_i \boldsymbol{\sigma}_i : \mathbb{C}^H(\mathbf{m}) : \boldsymbol{\sigma}_i \quad (\text{B.4})$$

$$\text{s.t. : } \mathbf{m} \in \mathcal{M}$$

This problem only requires low computational effort and can be solved with various optimization procedures³ in order to estimate the lower energy bounds for the load cases shown in figure 4. The resulting bounds are visualized for different volume fractions in figure B.8a. The optimal moments \mathbf{m}^* are invariant to the volume fraction \tilde{f} . For all loading scenarios depending on $\chi \in [0, 1]$ only m_3^* is varying ($m_1^* = m_2^* = m_4^* = 0$), see figure B.8b.

³Here, the SQP algorithm [47] of the MATLAB optimization toolbox with analytical gradient information and standard parameters is used.

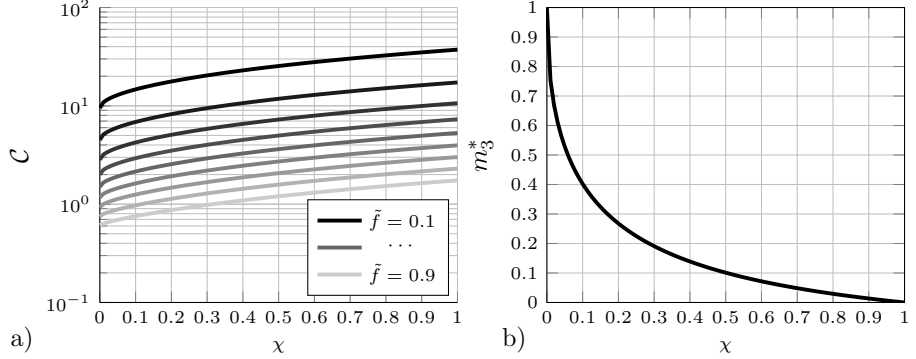


Figure B.8: a) Theoretical lower bounds for the complementary work \mathcal{C} for different volume fractions b) optimal moment m_3^* for all volume fractions of rank-N laminates.

Appendix C. Reconstructing rank-3

The parallelogram shown in figure C.9, representing a rank-3 laminate, is fully described by the relative layer spacing λ_i and the layer orientations θ_i .

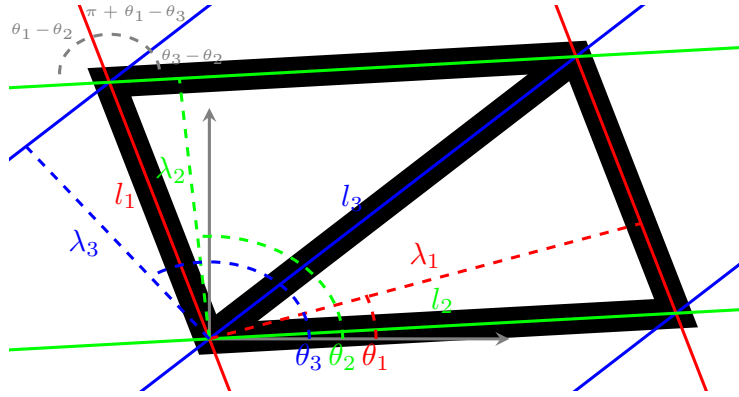


Figure C.9: Reconstructed rank-3 parallelogram.

255

Given one of the layer spacings, the others are defined in dependency of the orientations:

$$\boldsymbol{l} = \begin{bmatrix} \sqrt{l_2^2 + l_3^2 - 2l_2l_3 \cos(\theta_3 - \theta_2)} \\ \frac{\lambda_1}{|\sin(\theta_2 - \theta_1)|} \\ \frac{\lambda_1}{|\sin(\pi + \theta_1 - \theta_3)|} \end{bmatrix} \quad \boldsymbol{\lambda} = \begin{bmatrix} 1 \\ l_3 |\sin \theta_3 - \theta_2| \\ l_2 |\sin \theta_3 - \theta_2| \end{bmatrix} \quad (\text{C.1})$$

These spacings are normalized by the area of the unit cell $A = l_1 \lambda_1$. In order to reconstruct the layer orientations $\boldsymbol{\theta}$ based on the optimized moments m_i , the original four moments are rotated to configuration \tilde{m}_j by angle γ , so that $\tilde{m}_4 = 0$.

$$\gamma = \begin{cases} \frac{1}{4} \arctan -\frac{m_4}{m_3} & m_3 \neq 0 \\ \frac{\pi}{2} & m_3 = 0 \end{cases} \quad (\text{C.2a})$$

$$\tilde{\mathbf{m}} = \begin{bmatrix} m_1 \cos 2\gamma - m_2 \sin 2\gamma \\ m_2 \cos 2\gamma + m_1 \sin 2\gamma \\ m_3 \cos 4\gamma - m_4 \sin 4\gamma \end{bmatrix} \quad (\text{C.2b})$$

According to [16, 17] one solution for the layer orientations can be obtained by solving the following nonlinear equation for α , setting $\tilde{\mathbf{a}}$ to one of the corner points of the feasible set \tilde{M} , e.g. $\tilde{\mathbf{a}} = [1, 0, 1]$.

$$f(\alpha) = 2\tilde{b}_1^2(1 - \tilde{b}_3) + 2\tilde{b}_2^2(1 + \tilde{b}_3) + \tilde{b}_3^2 - 1 = 0 \quad (\text{C.3a})$$

$$\tilde{\mathbf{b}} = \frac{1}{1 - \alpha} [\tilde{\mathbf{m}} - \alpha \tilde{\mathbf{a}}] \quad (\text{C.3b})$$

The layer orientations and contributions for rank-2 and rank-3 laminates is now given by:

$$\mathbf{p}_2 = \begin{bmatrix} w \\ 1 - w \end{bmatrix} \quad \boldsymbol{\theta}_2 = \begin{bmatrix} \phi \\ \phi + \delta \end{bmatrix} - \gamma \quad (\text{C.4a})$$

$$\mathbf{p}_3 = \begin{bmatrix} \alpha \\ (1 - \alpha)\mathbf{p}_2 \end{bmatrix} \quad \boldsymbol{\theta}_3 = \begin{bmatrix} -\gamma \\ \boldsymbol{\theta}_2 \end{bmatrix} \quad (\text{C.4b})$$

$$s = \tilde{b}_3^2 - \frac{4\tilde{b}_1^2\tilde{b}_3}{1 + \tilde{b}_3} - \frac{4\tilde{b}_2^2\tilde{b}_3}{1 - \tilde{b}_3} + 1 \quad (\text{C.4c})$$

$$w = \frac{1}{2} + \frac{4\tilde{b}_1\tilde{b}_2\tilde{b}_3}{\sqrt{s(1 - \tilde{b}_3^2)}} \quad (\text{C.4d})$$

$$\delta = \arctan \sqrt{\frac{s}{1 - \tilde{b}_3^2}} \quad (\text{C.4e})$$

$$\phi = \arctan \frac{\tilde{b}_2 - (1 - w) \sin 2\delta}{w + (1 - w) \cos 2\delta + \tilde{b}_1} \quad (\text{C.4f})$$

Appendix D. Sensitivity analysis

The homogenized stiffness matrix is given by a sum over all integration points:

$$\mathbb{S}^H = \frac{1}{V} \sum_{i=1}^{n_e} \sum_{j=1}^{n_g} (\boldsymbol{\varepsilon}^0 - \mathbf{B}_j \boldsymbol{\chi})^T \mathbb{S}_i (\boldsymbol{\varepsilon}^0 - \mathbf{B}_j \boldsymbol{\chi}) \det J_j w_j \quad (\text{D.1})$$

Using the chain rule yields:

$$\begin{aligned} \frac{\partial \mathbb{S}^H}{\partial X_k} &= \frac{1}{V} \sum_{i=1}^{n_e} \sum_{j=1}^{n_g} \frac{\partial (\boldsymbol{\varepsilon}^0 - \mathbf{B}_j \boldsymbol{\chi})^T}{\partial X_k} \mathbb{S}_i (\boldsymbol{\varepsilon}^0 - \mathbf{B}_j \boldsymbol{\chi}) \det J_j w_j + \\ &\quad (\boldsymbol{\varepsilon}^0 - \mathbf{B}_j \boldsymbol{\chi})^T \mathbb{S}_i \frac{\partial (\boldsymbol{\varepsilon}^0 - \mathbf{B}_j \boldsymbol{\chi})}{\partial X_k} \det J_j w_j + \\ &\quad (\boldsymbol{\varepsilon}^0 - \mathbf{B}_j \boldsymbol{\chi})^T \mathbb{S}_i (\boldsymbol{\varepsilon}^0 - \mathbf{B}_j \boldsymbol{\chi}) \frac{\partial \det J_j}{\partial X_k} w_j \end{aligned} \quad (\text{D.2})$$

The first term can be written as:

$$\begin{aligned} &\sum_{i=1}^{n_e} \sum_{j=1}^{n_g} \frac{\partial (\boldsymbol{\varepsilon}^0 - \mathbf{B}_j \boldsymbol{\chi}_i)^T}{\partial X_k} \mathbb{S}_i (\boldsymbol{\varepsilon}^0 - \mathbf{B}_j \boldsymbol{\chi}_i) \det J_j w_j \\ &= -\boldsymbol{\chi}^T \sum_{i=1}^{n_e} \sum_{j=1}^{n_g} \frac{\partial \mathbf{B}_j^T}{\partial X_k} \mathbb{S}_i (\boldsymbol{\varepsilon}^0 - \mathbf{B}_j \boldsymbol{\chi}_i) \det J_j w_j \\ &\quad - \underbrace{\frac{\partial \boldsymbol{\chi}^T}{\partial X_k} \sum_{i=1}^{n_e} \sum_{j=1}^{n_g} \mathbf{B}_j^T \mathbb{S}_i (\boldsymbol{\varepsilon}^0 - \mathbf{B}_j \boldsymbol{\chi}_i) \det J_j w_j}_{\boldsymbol{\kappa}_{\boldsymbol{\chi}} - \boldsymbol{P} = \mathbf{0}} \end{aligned} \quad (\text{D.3})$$

The derivatives of the B-Matrices and the JACOBIAN determinant follow directly from the second derivative of the shape functions:

$$\frac{\partial \nabla_{\mathbf{X}} \mathbf{N}}{\partial X_k} = \nabla_{\mathbf{X}} \mathbf{N}_k \mathbf{e}_k^T \nabla_{\mathbf{X}} \mathbf{N} \quad (\text{D.4})$$

$$\frac{\partial \det \mathbf{J}}{\partial X_k} = \det \mathbf{J} \left(\mathbf{J}^{-T} : \nabla_{\boldsymbol{\xi}} \mathbf{N}_k \mathbf{e}_k^T \right) \quad (\text{D.5})$$

Appendix E. Stress evaluation

Starting from the correction displacement fields, which are estimated during the numerical homogenization using three load cases (2D), one can compute the

effective stresses for an applied stress state. The stress at the local position ξ for the three test load cases is given by:

$$\boldsymbol{\sigma}_i^0(\xi) = \mathbb{S}(\boldsymbol{\varepsilon}_i^0 - \mathbf{B}(\xi)\boldsymbol{\chi}_i) \quad (\text{E.1})$$

The effective global stress states for these test load cases follows from the homogenized material tensor:

$$\boldsymbol{\sigma}_i^0 = \mathbb{S}^H \boldsymbol{\varepsilon}_i^0 \quad (\text{E.2})$$

The applied global stress vector for is the sum of the n_σ applied weighted stress vectors $\boldsymbol{\sigma}_I$:

$$\boldsymbol{\sigma}^a = \sum_{I=1}^{n_\sigma} w_I \boldsymbol{\sigma}_I \quad (\text{E.3})$$

Now one could solve for $\boldsymbol{\alpha}$:

$$\begin{bmatrix} \boldsymbol{\sigma}_1^0 & \boldsymbol{\sigma}_2^0 & \boldsymbol{\sigma}_3^0 \end{bmatrix} \boldsymbol{\alpha} = \boldsymbol{\sigma}^a \Rightarrow \boldsymbol{\alpha} = \mathbb{C}^H \boldsymbol{\sigma}^a \quad (\text{E.4})$$

Considering linear elasticity, the local stresses for the applied stress vector $\boldsymbol{\sigma}^a$ are now a linear combination from the local stresses estimated for the test load cases:

$$\boldsymbol{\sigma}(\xi) = \sum_{i=1}^3 \alpha_i \boldsymbol{\sigma}_i^0(\xi) \quad (\text{E.5})$$

The VON MISES-stress is given by:

$$\sigma_{VM}(\boldsymbol{\sigma}) = \sqrt{\sigma_{11}^2 + \sigma_{22}^2 - \sigma_{11}\sigma_{22} + 3\sigma_{12}^2} \quad (\text{E.6})$$

References

- [1] M. P. Bendsøe, O. Sigmund, Material interpolation schemes in topology optimization, Archive of Applied Mechanics 69 (9-10) (1999) 635–654. doi: 10.1007/s004190050248.
- [2] O. Sigmund, K. Maute, Topology optimization approaches, Structural and Multidisciplinary Optimization 48 (6) (2013) 1031–1055. doi:10.1007/s00158-013-0978-6.

- 265 [3] Z. Hashin, S. Shtrikman, A variational approach to the theory of the elastic behaviour of multiphase materials, *Journal of the Mechanics and Physics of Solids* 11 (2) (1963) 127–140. doi:10.1016/0022-5096(63)90060-7.
- 270 [4] A. V. Cherkaev, L. V. Gibiansky, Coupled estimates for the bulk and shear moduli of a two-dimensional isotropic elastic composite, *Journal of the Mechanics and Physics of Solids* 41 (5) (1993) 937–980. doi:10.1016/0022-5096(93)90006-2.
- 275 [5] O. Sigmund, A new class of extremal composites, *Journal of the Mechanics and Physics of Solids* 48 (2) (2000) 397–428. doi:10.1016/S0022-5096(99)00034-4.
- [6] R. Sivapuram, P. D. Dunning, H. A. Kim, Simultaneous material and structural optimization by multiscale topology optimization, *Structural and Multidisciplinary Optimization* 54 (5) (2016) 1267–1281. doi:10.1007/s00158-016-1519-x.
- 280 [7] J. P. Groen, O. Sigmund, Homogenization-based topology optimization for high-resolution manufacturable micro-structures, *International Journal for Numerical Methods in Engineering* (2017) n/a–n/a doi:10.1002/nme.5575.
- 285 [8] B. Hassani, E. Hinton, A review of homogenization and topology optimization I—homogenization theory for media with periodic structure, *Computers & Structures* 69 (6) (1998) 707–717. doi:10.1016/S0045-7949(98)00131-X.
- [9] B. Hassani, E. Hinton, A review of homogenization and topology optimization III—topology optimization using optimality criteria, *Computers & Structures* 69 (6) (1998) 739–756. doi:10.1016/S0045-7949(98)00133-3.
- 290 [10] E. Andreassen, C. S. Andreasen, How to determine composite material properties using numerical homogenization, *Computational Materials Science* 83 (2014) 488–495. doi:10.1016/j.commatsci.2013.09.006.

- [11] O. Sigmund, Materials with prescribed constitutive parameters: An inverse homogenization problem, *International Journal of Solids and Structures* 31 (17) (1994) 2313–2329. doi:[10.1016/0020-7683\(94\)90154-6](https://doi.org/10.1016/0020-7683(94)90154-6).
- [12] O. Sigmund, Design of material structures using topology optimization, Ph.D. thesis, Technical University of Denmark (1994).
- [13] O. Sigmund, Tailoring materials with prescribed elastic properties, *Mechanics of Materials* 20 (4) (1995) 351–368. doi:[10.1016/0167-6636\(94\)00069-7](https://doi.org/10.1016/0167-6636(94)00069-7).
- [14] M. Osanov, J. K. Guest, Topology Optimization for Architected Materials Design, *Annual Review of Materials Research* 46 (1) (2016) 211–233. doi:[10.1146/annurev-matsci-070115-031826](https://doi.org/10.1146/annurev-matsci-070115-031826).
- [15] E. Träff, O. Sigmund, J. P. Groen, Simple single-scale microstructures based on optimal rank-3 laminates, *Structural and Multidisciplinary Optimization* (Jan. 2019). doi:[10.1007/s00158-018-2180-3](https://doi.org/10.1007/s00158-018-2180-3).
- [16] R. Lipton, On optimal reinforcement of plates and choice of design parameters, *Control and Cybernetics* 23 (1994) 14.
- [17] A. R. Diaz, R. Lipton, C. A. Soto, A new formulation of the problem of optimum reinforcement of Reissner-Mindlin plates, *Computer Methods in Applied Mechanics and Engineering* 123 (1) (1995) 121–139. doi:[10.1016/0045-7825\(94\)00777-K](https://doi.org/10.1016/0045-7825(94)00777-K).
- [18] G. Allaire, P. Geoffroy-Donders, O. Pantz, Topology optimization of modulated and oriented periodic microstructures by the homogenization method, *Computers & Mathematics with Applications* (Aug. 2018). doi:[10.1016/j.camwa.2018.08.007](https://doi.org/10.1016/j.camwa.2018.08.007).
- [19] V. Braibant, C. Fleury, Shape optimal design using B-splines, *Computer Methods in Applied Mechanics and Engineering* 44 (3) (1984) 247–267. doi:[10.1016/0045-7825\(84\)90132-4](https://doi.org/10.1016/0045-7825(84)90132-4).

- 320 [20] C. Le, T. Bruns, D. Tortorelli, A gradient-based, parameter-free approach
to shape optimization, Computer Methods in Applied Mechanics and En-
gineering 200 (9) (2011) 985–996. doi:[10.1016/j.cma.2010.10.004](https://doi.org/10.1016/j.cma.2010.10.004).
- 325 [21] E. Cohen, T. Martin, R. M. Kirby, T. Lyche, R. F. Riesenfeld, Analysis-
aware modeling: Understanding quality considerations in modeling for iso-
geometric analysis, Computer Methods in Applied Mechanics and Engi-
neering 199 (5) (2010) 334–356. doi:[10.1016/j.cma.2009.09.010](https://doi.org/10.1016/j.cma.2009.09.010).
- [22] R. T. Haftka, R. V. Grandhi, Structural shape optimization—A survey,
Computer Methods in Applied Mechanics and Engineering 57 (1) (1986)
91–106. doi:[10.1016/0045-7825\(86\)90072-1](https://doi.org/10.1016/0045-7825(86)90072-1).
- 330 [23] M. Firl, R. Wüchner, K.-U. Bletzinger, Regularization of shape op-
timization problems using FE-based parametrization, Structural and
Multidisciplinary Optimization 47 (4) (2013) 507–521. doi:[10.1007/s00158-012-0843-z](https://doi.org/10.1007/s00158-012-0843-z).
- 335 [24] M. Hojjat, E. Stavropoulou, K.-U. Bletzinger, The Vertex Morphing
method for node-based shape optimization, Computer Methods in Ap-
plied Mechanics and Engineering 268 (2014) 494–513. doi:[10.1016/j.cma.2013.10.015](https://doi.org/10.1016/j.cma.2013.10.015).
- 340 [25] K.-U. Bletzinger, A consistent frame for sensitivity filtering and the ver-
tex assigned morphing of optimal shape, Structural and Multidisciplinary
Optimization 49 (6) (2014) 873–895. doi:[10.1007/s00158-013-1031-5](https://doi.org/10.1007/s00158-013-1031-5).
- [26] L. Piegl, W. Tiller, The NURBS Book, Springer Science & Business Media,
1997.
- 345 [27] T. W. Sederberg, J. Zheng, A. Bakenov, A. Nasri, T-splines and T-
NURCCs, in: ACM SIGGRAPH 2003 Papers, SIGGRAPH '03, ACM, New
York, NY, USA, 2003, pp. 477–484. doi:[10.1145/1201775.882295](https://doi.org/10.1145/1201775.882295).
- [28] T. J. R. Hughes, J. A. Cottrell, Y. Bazilevs, Isogeometric analysis: CAD,
finite elements, NURBS, exact geometry and mesh refinement, Computer

- Methods in Applied Mechanics and Engineering 194 (39) (2005) 4135–4195.
doi:10.1016/j.cma.2004.10.008.
- [29] W. A. Wall, M. A. Frenzel, C. Cyron, Isogeometric structural shape optimization, Computer Methods in Applied Mechanics and Engineering 197 (33) (2008) 2976–2988. doi:10.1016/j.cma.2008.01.025.
- [30] Y.-D. Seo, H.-J. Kim, S.-K. Youn, Shape optimization and its extension to topological design based on isogeometric analysis, International Journal of Solids and Structures 47 (11–12) (2010) 1618–1640. doi:10.1016/j.ijsolstr.2010.03.004.
- [31] D. Fußeder, B. Simeon, A. V. Vuong, Fundamental aspects of shape optimization in the context of isogeometric analysis, Computer Methods in Applied Mechanics and Engineering 286 (2015) 313–331. doi:10.1016/j.cma.2014.12.028.
- [32] Y. Wang, Z. Wang, Z. Xia, L. Hien Poh, Structural Design Optimization Using Isogeometric Analysis: A Comprehensive Review, Computer Modeling in Engineering & Sciences 117 (3) (2018) 455–507. doi:10.31614/cmes.2018.04603.
- [33] X. Qian, O. Sigmund, Isogeometric shape optimization of photonic crystals via Coons patches, Computer Methods in Applied Mechanics and Engineering 200 (25-28) (2011) 2237–2255. doi:10.1016/j.cma.2011.03.007.
- [34] Z.-P. Wang, L. H. Poh, J. Dirrenberger, Y. Zhu, S. Forest, Isogeometric shape optimization of smoothed petal auxetic structures via computational periodic homogenization, Computer Methods in Applied Mechanics and Engineering 323 (2017) 250–271. doi:10.1016/j.cma.2017.05.013.
- [35] C. Wang, S. Xia, X. Wang, X. Quian, Isogeometric shape optimization on triangulations, Computer Methods in Applied Mechanics and Engineering 331 (2018) 585–622. doi:10.1016/j.cma.2017.11.032.

- 375 [36] P. Wriggers, Nonlinear Phenomena, in: Nonlinear Finite Element Methods, Springer Berlin Heidelberg, 2008, pp. 7–18. doi:10.1007/978-3-540-71001-1_2.
- 380 [37] J. A. Cottrell, T. J. R. Hughes, Y. Bazilevs, Isogeometric Analysis: Toward Integration of CAD and FEA, 1st Edition, Wiley, Chichester, West Sussex, U.K. ; Hoboken, NJ, 2009.
- 385 [38] V. P. Nguyen, C. Anitescu, S. P. A. Bordas, T. Rabczuk, Isogeometric analysis: An overview and computer implementation aspects, Mathematics and Computers in Simulation 117 (2015) 89–116. doi:10.1016/j.matcom.2015.05.008.
- 390 [39] T. Hughes, A. Reali, G. Sangalli, Efficient quadrature for NURBS-based isogeometric analysis, Computer Methods in Applied Mechanics and Engineering 199 (5-8) (2010) 301–313. doi:10.1016/j.cma.2008.12.004.
- [40] J. A. Cottrell, T. J. R. Hughes, A. Reali, Studies of refinement and continuity in isogeometric structural analysis, Computer Methods in Applied Mechanics and Engineering 196 (41) (2007) 4160–4183. doi:10.1016/j.cma.2007.04.007.
- 41] B.-G. Lee, Y. Park, Degree elevation of nurbs curves by weighted blossom, Korean Journal of Computational & Applied Mathematics 9 (1) (2002) 151–165. doi:10.1007/BF03012346.
- 395 [42] J. A. Samareh, Survey of Shape Parameterization Techniques for High-Fidelity Multidisciplinary Shape Optimization, AIAA Journal 39 (5) (2001) 877–884. doi:10.2514/2.1391.
- [43] E. Lund, Finite Element Based Design Sensitivity Analysis and Optimization, Ph.D. thesis, Aalborg University (1994).
- 400 [44] F. van Keulen, R. Haftka, N. Kim, Review of options for structural design sensitivity analysis. Part 1: Linear systems, Computer Methods in Applied

- Mechanics and Engineering 194 (30-33) (2005) 3213–3243. doi:10.1016/j.cma.2005.02.002.
- [45] O. Sigmund, On the usefulness of non-gradient approaches in topology optimization, Structural and Multidisciplinary Optimization 43 (5) (2011) 589–596. doi:10.1007/s00158-011-0638-7.
- [46] K. Svanberg, The method of moving asymptotes - a new method for structural optimization, International Journal for Numerical Methods in Engineering 24 (2) (1987) 359–373. doi:10.1002/nme.1620240207.
- [47] J. Nocedal, S. J. Wright, Numerical Optimization, Springer Series in Operations Research and Financial Engineering, Springer New York, 2006.
- [48] J. Guedes, H. Rodrigues, M. Bendsøe, A material optimization model to approximate energy bounds for cellular materials under multiload conditions, Structural and Multidisciplinary Optimization 25 (5) (2003) 446–452. doi:10.1007/s00158-003-0305-8.
- [49] S. B. Vigdergauz, Regular structures with extremal elastic properties, Mechanics of Solids 24 (3) (1989) 57.